

Two-dimensional kagome semiconductor $Sc_6S_5X_6$ (X = Cl, Br, I) with trilayer kagome lattice

Jin-Ling Yan(闫金铃), Xing-Yu Wang(王星雨), Gen-Ping Wu(吴根平), Hao Wang(王浩), Ya-Jiao Ke(柯亚娇), Jiafu Wang(王嘉赋), Zhi-Hong Liu(刘志宏), and Jun-Hui Yuan(袁俊辉)

Citation: Chin. Phys. B, 2026, 35 (**2**): 027102. DOI: 10.1088/1674-1056/ae00b4
http://cpb.iphy.ac.cn; http://iopscience.iop.org/cpb

What follows is a list of articles you may be interested in

Unique high-energy excitons in two-dimensional transition metal dichalcogenides

Yongsheng Gao(高永盛), Yuanzheng Li(李远征), Weizhen Liu(刘为振), Chuxin Yan(闫楚欣), Qingbin Wang(王庆彬), Wei Xin(辛巍), Haiyang Xu(徐海阳), and Yichun Liu(刘益春)

Chin. Phys. B, 2025, 34 (**9**): 097102. DOI: 10.1088/1674-1056/ade074

Anomalous ultrafast thermalization of photoexcited carriers in two-dimensional materials induced by orbital coupling

Zhuoqun Wen(文卓群), Haiyu Zhu(诸海渝), Wen-Hao Liu(刘文浩), Zhi Wang(王峙), Wen Xiong(熊稳), and Xingzhan Wei(魏兴战)

Chin. Phys. B, 2025, 34 (**7**): 077103. DOI: 10.1088/1674-1056/adc191

Unveiling the thermal transport mechanisms in novel carbon-based graphene-like materials using machine-learning potential

Yao-Yuan Zhang(章耀元), Meng-Qiu Long(龙孟秋), Sai-Jie Cheng(程赛杰), and Wu-Xing Zhou(周五星)

Chin. Phys. B, 2025, 34 (**6**): 067101. DOI: 10.1088/1674-1056/adca18

High-temperature ferromagnetism and strong π-conjugation feature in two-dimensional manganese tetranitride

Ming Yan(闫明), Zhi-Yuan Xie(谢志远), and Miao Gao(高淼)

Chin. Phys. B, 2023, 32 (**3**): 037104. DOI: 10.1088/1674-1056/acae7b

Two ultra-stable novel allotropes of tellurium few-layers

Changlin Yan(严长林), Cong Wang(王聪), Linwei Zhou(周霖蔚), Pengjie Guo(郭朋杰), Kai Liu(刘凯), Zhong-Yi Lu(卢仲毅), Zhihai Cheng(程志海), Yang Chai(柴扬), Anlian Pan(潘安练), Wei Ji(季威)

Chin. Phys. B, 2020, 29 (**9**): 097103. DOI: 10.1088/1674-1056/aba606

Two-dimensional kagome semiconductor $Sc_6S_5X_6$ (X = Cl, Br, I) with trilayer kagome lattice

Jin-Ling Yan(闫金铃)[1,†], Xing-Yu Wang(王星雨)[1,2,†], Gen-Ping Wu(吴根平)[3], Hao Wang(王浩)[3], Ya-Jiao Ke(柯亚娇)[1,‡], Jiafu Wang(王嘉赋)[1], Zhi-Hong Liu(刘志宏)[3,§], and Jun-Hui Yuan(袁俊辉)[1,¶]

[1] *School of Physics and Mechanics, Wuhan University of Technology, Wuhan* 430070, *China*
[2] *School of Materials and Microelectronics, Wuhan University of Technology, Wuhan* 430070, *China*
[3] *Wuhan Second Ship Design and Research Institute, Wuhan* 430205, *China*

(Received 5 August 2025; revised manuscript received 28 August 2025; accepted manuscript online 29 August 2025)

Two-dimensional (2D) multilayer kagome materials hold significant research value for regulating kagome-related physical properties and exploring quantum effects. However, their development is hindered by the scarcity of available material systems, making the identification of novel 2D multilayer kagome candidates particularly important. In this work, three types of 2D materials with trilayer kagome lattices, namely $Sc_6S_5X_6$ (X = Cl, Br, I), are predicted based on first-principles calculations. These 2D materials feature two kagome lattices composed of Sc atoms and one kagome lattice composed of S atoms. Stability analysis indicates that these materials can exist as free-standing 2D materials. Electronic structure calculations reveal that $Sc_6S_5X_6$ are narrow-bandgap semiconductors (0.76–0.95 eV), with their band structures exhibiting flat bands contributed by Sc-based kagome lattices and Dirac band gaps resulting from symmetry breaking. The sulfur-based kagome lattice in the central layer contributes an independent flat band below the Fermi level. Additionally, $Sc_6S_5X_6$ exhibit high carrier mobility, with hole and electron mobilities reaching up to 10^3 $cm^2 \cdot V^{-1} \cdot s^{-1}$, indicating potential applications in low-dimensional electronic devices. This work provides an excellent example for the development of novel multilayer 2D kagome materials.

Keywords: multilayer kagome lattice, two-dimensional materials, carrier mobility, first-principles calculations

PACS: 71.18.+y, 71.20.–b

DOI: 10.1088/1674-1056/ae00b4 **CSTR:** 32038.14.CPB.ae00b4

1. Introduction

Two-dimensional (2D) materials have become a cutting-edge frontier in numerous contemporary disciplines and applied research fields.[1–3] This is because, compared to traditional three-dimensional (3D) materials, the reduction in dimensionality in 2D materials makes the associated quantum effects more pronounced.[4–7] Many physical properties that are difficult to capture in traditional materials can be effectively observed and further exploited in 2D materials. Consequently, current research on 2D materials primarily follows two paths: one is to conduct in-depth investigations into 2D materials that have been successfully synthesized experimentally, aiming to unearth their latent potential; the other is to continuously explore and develop novel 2D materials, injecting a steady stream of vitality into the future development of this field.

Amidst the current research fervor surrounding 2D materials, 2D kagome materials stand out as a rising star, attracting widespread attention.[8,9] Kagome materials derive their name from their unique kagome lattice structure, which consists of two opposing triangular lattices and represents a highly representative lattice type in physics. Ideal kagome lattices possess a series of distinctive physical properties, such as flat bands, Dirac cones, and van Hove singularities.[10] These properties provide a fertile ground for the emergence of various other physical phenomena, offering potential platforms for superconductivity, strongly correlated physics, magnetism, topology, and many other physical characteristics.[11–16] However, ideal kagome lattices often struggle to maintain stability in reality, necessitating the introduction of foreign elements for passivation or protection to enhance their stability. Currently, materials such as M_3QX_7 (M = Nb, Ta; Q = S, Se, Te; X = Cl, Br, I),[17] M_3X_8 (M = Ti, V, Nb, Ta; X = Cl, Br, I),[18–22] TMO monolayers (TM = transition metal)[23] and M_2X_3 (M = P, Mo, Ti, Zr, Hf, V, Nb, Ta; X = C, O_2, Se, C_6H_4)[24–27] have garnered significant attention in the realm of 2D kagome material research. Nevertheless, it is noteworthy that most current research focuses on single-layer kagome systems,[28–31] with relatively limited exploration of multilayer kagome systems. In fact, multilayer kagome systems may harbor even more unexplored and exceptional properties. On one hand, multilayer kagome lattices increase the degrees of freedom in spatial di-

[†]These authors contributed equally to this work.
[‡]Corresponding author. E-mail: keyajiao@whut.edu.cn
[§]Corresponding author. E-mail: 54181880@qq.com
[¶]Corresponding author. E-mail: yuanjh90@163.com

© 2026 Chinese Physical Society and IOP Publishing Ltd. All rights, including for text and data mining, AI training, and similar technologies, are reserved.

mensions, providing new opportunities for the discovery of novel phenomena and the emergence of new properties; on the other hand, multilayer kagome lattices require the introduction of additional passivation atoms, offering favorable conditions for the precise regulation of their related properties. Therefore, conducting research on 2D multilayer kagome materials holds crucial significance for driving the sustained development of this field.

In this study, we take the 2D bilayer kagome material $Sc_6S_6X_6$ (X = Cl, Br, I), proposed earlier by our research group,[32] as the research object. By ingeniously introducing specific sulfur vacancies, the bilayer kagome material $Sc_6S_6X_6$ is successfully transformed into a novel 2D material $Sc_6S_5X_6$ with three kagome layers. Theoretical results demonstrate that $Sc_6S_5X_6$ not only exhibits excellent stability but also functions as a narrow-bandgap semiconductor. In its electronic structure, kagome band features contributed by the three kagome lattices are prominently evident, making it a highly promising candidate for 2D kagome semiconductors. More detailed research findings on this material will be presented step by step in Section 3.

2. Computational method

The projector augmented wave (PAW) method[33,34] implemented in Vienna *ab initio* simulation package (VASP)[35,36] has been employed for the calculations, with the valence electron configurations for Sc, S, Cl, Br, and I being $3d^14s^2$, $3s^23p^4$, $3s^23p^5$, $4s^24p^5$, and $5s^25p^5$, respectively. The plane-wave cutoff energy was set to 500 eV. The exchange-correlation energy was treated using the generalized gradient approximation (GGA) in the Perdew–Burke–Ernzerhof (PBE) form.[37] For structural optimization and static self-consistency, $9\times9\times1$ and $11\times11\times1$ Gamma-centered k-point grids were used, respectively, with force and energy convergence criteria of 0.002 eV/Å and 10^{-7} eV, respectively. For all 2D $Sc_6S_5X_6$ structures, a vacuum slab with a thickness of 20 Å was incorporated along the z-direction to prevent interactions between adjacent layers. To assess the thermodynamic stability of 2D $Sc_6S_5X_6$, *ab initio* molecular dynamics (AIMD) simulations were conducted for a duration of 5 ps at temperatures ranging from 300 K to 800 K. Additionally, the LOBSTER software was employed to analyze chemical bonding properties.[38] Phonon dispersions, based on density functional perturbation theory (DFPT), were calculated using the Phonopy code.[39] The VASPKIT code was utilized during data pre- and post-processing.[40]

3. Results and discussion

3.1. Structure and stability

In our previous work, a novel scandium-based 2D material, $Sc_6S_6X_6$ (X = Cl, Br, I), featuring a bilayer kagome lattice, was successfully designed by employing surface passivation and charge balance strategies, as shown in Fig. 1(a). Based on spatial symmetry analysis, within the $Sc_6S_6X_6$ monolayer, sulfur atoms occupy three non-equivalent sites, labeled as S1, S2, and S3, with their specific positions depicted in Fig. 1(a). Among them, S1 atoms are precisely located directly above and below the centers of the triangular sublattices within the upper and lower kagome layers. The atomic layer composed of S2 and S3 atoms is situated between the two kagome layers, with the specific structure illustrated in Fig. 1(b). Meanwhile, halogen atoms are distributed on the outer side of the kagome layers, forming a passivation layer that serves to protect and stabilize the material.

From the perspective of crystal structure details, the central layer of $Sc_6S_6X_6$ is composed of four sulfur atoms lying in the same plane. Among these four sulfur atoms, three equivalent S2 atoms form the fundamental framework of the kagome lattice, while the remaining S3 atom is positioned at the center of the hexagonal ring within the kagome lattice. This unique configuration renders the kagome lattice imperfect, as shown in Fig. 1(b). Based on this observation, we hypothesize that if the S3 atom is removed (as depicted in Fig. 1(c)), a perfect kagome lattice composed of S2 atoms can be formed in the central layer (as shown in Fig. 1(d)), thereby providing an ideal model for investigating the physical properties of multilayer kagome lattice systems.

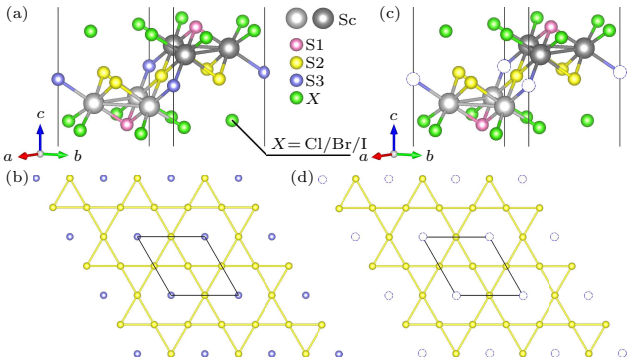


Fig. 1. (a) Schematic diagram of $Sc_6S_6X_6$ and (b) the central sulfur-atom layer of $Sc_6S_6X_6$. (c) Side view of $Sc_6S_5X_6$, where the blue dashed spheres represent sulfur-atom vacancies. (d) Schematic diagram of the central sulfur-atom layer of $Sc_6S_5X_6$ after introducing an S3 vacancy.

Table 1 provides a detailed summary of the optimized lattice constants (a/b), corresponding bond lengths (Sc–S1, Sc–S2, Sc–X, Sc–Sc), and other relevant parameters for the designed $Sc_6S_5X_6$ monolayer. The results reveal that, among the three compounds, the bond lengths of Sc–S1 (d_1) and Sc–S2 (d_2) remain relatively stable, whereas the bond length of Sc–X (d_3) exhibits a notable increasing trend. Additionally, the difference between the short bond (l_1) and the long bond (l_2) of the Sc–Sc bonds constituting the triangular sublattice becomes increasingly pronounced, as illustrated by the bond-length schematic shown in Fig. S1.

Table 1. Structural parameters and band gap values of $Sc_6S_5X_6$ monolayer.

Materials	a/b	d_1	d_2	d_3	l_1/l_2	E_g^{PBE}	$E_g^{PBE+SOC}$	E_g^{HSE}	$E_g^{HSE+SOC}$
$Sc_6S_5Cl_6$	7.43	2.45	2.58	2.48	3.51/3.92	0.46	0.46	0.97	0.95
$Sc_6S_5Br_6$	7.56	2.45	2.58	2.64	3.52/4.04	0.43	0.42	0.92	0.91
$Sc_6S_5I_6$	7.85	2.45	2.6	2.87	3.54/4.31	0.33	0.32	0.75	0.76

It is noteworthy that after the removal of S3 atoms, the bond lengths of Sc–S1 (d_1), Sc–S2 (d_2), and Sc–X (d_3) all increase compared to those in the $Sc_6S_6X_6$ monolayer, with increments of approximately 0.01 Å to 0.02 Å. Additionally, the length of the Sc–Sc (l_1) bond is shorter than that of the l_1 bond in the $Sc_6S_6X_6$ monolayer, while the length of the Sc–Sc (l_2) bond is longer than that of the l_2 bond in the $Sc_6S_6X_6$ monolayer. Consequently, the difference between l_1 and l_2 further widens after the introduction of S vacancies, indicating that the two triangular sublattices in the Sc-based kagome lattice are further stretched. As a result, the lattice constants a/b of the entire $Sc_6S_5X_6$ monolayer also increase by 0.06 Å to 0.14 Å, as detailed in Table S1.

Verifying the stability of newly predicted materials holds paramount significance for advancing subsequent research endeavors. Consequently, we undertook a comprehensive examination of the stability of the $Sc_6S_5X_6$ monolayer from kinetic, thermodynamic, and mechanical perspectives. Initially, phonon dispersions of the $Sc_6S_5X_6$ monolayer were calculated using a $2\times2\times1$ supercell composed of 68 atoms. As shown in Figs. 2(a)–2(c), the absence of imaginary frequencies in the phonon spectra indicates that all $Sc_6S_5X_6$ monolayers exhibit excellent kinetic stability. From $Sc_6S_5Cl_6$ to $Sc_6S_5I_6$, as the atomic number of X increases, the phonon frequency range gradually narrows, and the degree of overlap among vibration modes increases.

Subsequently, we evaluated the thermal stability of $Sc_6S_5X_6$ within the temperature range of 300 K to 800 K. For this purpose, AIMD simulations using a $3\times3\times1$ supercell containing 153 atoms were performed, with the simulation results shown in Figs. 2(d)–2(f). After conducting 5 ps AIMD simulations at each temperature, the $Sc_6S_5Cl_6$ and $Sc_6S_5Br_6$ monolayers can maintain structural stability at temperatures up to 800 K, while the $Sc_6S_5I_6$ monolayer remains stable at 500 K, a temperature range that already satisfies the operational requirements of the vast majority of electronic devices. However, compared to the $Sc_6S_6X_6$ monolayer, the thermal stability of $Sc_6S_5X_6$ is reduced (the AIMD results for $Sc_6S_6X_6$ are shown in Fig. S2). After in-depth analysis, two primary reasons are identified. First, the introduction of S vacancies induces a localization effect. After removing the S atoms at the four vertices, the resulting vacancies cause the surrounding atoms to contract toward the vacancy centers, generating local compressive stress. During the AIMD simulations, thermal fluctuations amplify this stress, leading to increased oscillation amplitudes of atomic positions and ultimately resulting in structural collapse. Second, from an energy perspective, in $Sc_6S_6X_6$, each S3 atom at the vertices forms bonds with two neighboring Sc atoms above and below. However, removing the S3 atoms causes these bonds to break, forming dangling bonds. The surrounding atoms may partially compensate for these dangling bonds, potentially leading to bond-angle distortions and a significant increase in the enthalpy (ΔH) of the system. Consequently, the free energy (ΔG) of the entire system rises, as detailed in Table S2, thereby reducing the thermal stability of the $Sc_6S_5X_6$ monolayer.

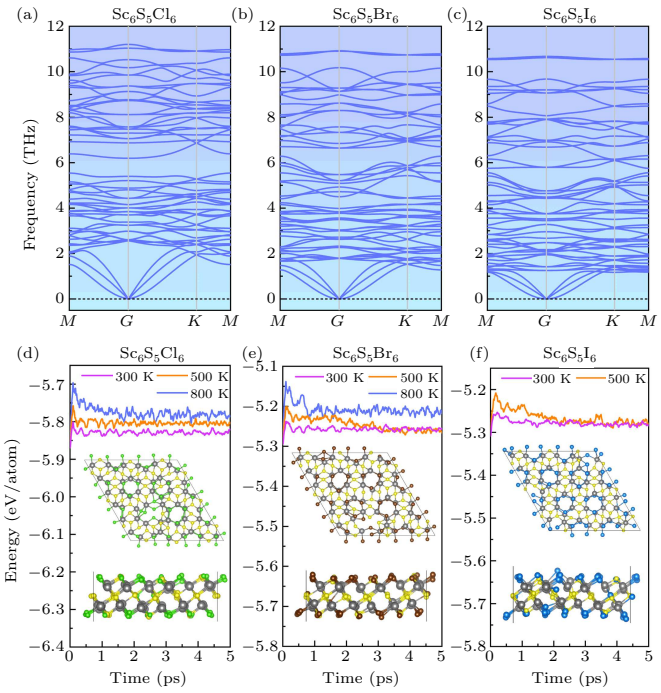


Fig. 2. Phonon dispersion and AIMD simulation results of $Sc_6S_5X_6$ monolayer. Phonon dispersion of (a) $Sc_6S_5Cl_6$, (b) $Sc_6S_5Br_6$, and (c) $Sc_6S_5I_6$. AIMD simulation results of (d) $Sc_6S_5Cl_6$, (e) $Sc_6S_5Br_6$, and (f) $Sc_6S_5I_6$. The insert is the final crystal structure after the simulations (800 K for $Sc_6S_5Cl_6$ and $Sc_6S_5Br_6$, 500 K for $Sc_6S_5I_6$).

In addition, to comprehensively evaluate the mechanical stability of the $Sc_6S_5X_6$ monolayer, its elastic constants have also been precisely calculated. For a 2D trigonal lattice, its independent elastic constants include C_{11} (where $C_{11}=C_{22}$), C_{12}, and C_{66}. According to the well-known Born–Huang criterion,[41] for a 2D material to possess mechanical stability, it must strictly satisfy the following two conditions: $C_{11}^2-C_{12}^2>0$ and $C_{66}>0$. After meticulous calculations, the independent elastic constants for the $Sc_6S_5X_6$ monolayer are summarized in Table S3. From the data in the table, it is evident that all three monolayers conform to the Born–Huang criterion, which demonstrates their excellent mechanical stability. These results further confirm that the $Sc_6S_5X_6$ monolayer

can stably exist as a free-standing 2D material under environmental conditions above room temperature.

Finally, using the calculated elastic constants, the Young's modulus (Y) and Poisson's ratio (v) of the $Sc_6S_5X_6$ monolayer were further evaluated. The relevant results are shown in Fig. 3, and the specific calculation method is described in Note 1 of the supplementary materials. The computational results demonstrate that 2D $Sc_6S_5X_6$ possesses isotropic mechanical properties. The Y of the $Sc_6S_5X_6$ monolayer lies within the range of 42.81 $N{\cdot}m^{-1}$ ($Sc_6S_5I_6$) to 48.69 $N{\cdot}m^{-1}$ ($Sc_6S_5Cl_6$). Compared to MoS_2 (180 $N{\cdot}m^{-1}$)[42] and graphene (342.2 $N{\cdot}m^{-1}$),[43] these values are significantly lower, indicating that $Sc_6S_5X_6$ exhibits higher flexibility than 2D materials such as MoS_2 and graphene. Meanwhile, the v of the corresponding $Sc_6S_5X_6$ monolayer ranges from 0.154 ($Sc_6S_5Cl_6$) to 0.163 ($Sc_6S_5Br_6$), which is slightly lower than that of some common 2D materials, such as graphene (0.175) and MoS_2 (0.21).[44] Materials with both low Young's modulus and moderate Poisson's ratio can effectively suppress surface cracking when devices are bent in practical applications, maintaining good flexibility while ensuring shape stability.

It is also noteworthy that compared to the $Sc_6S_6X_6$ monolayer, the elastic constants, Young's modulus, and Poisson's ratio of the $Sc_6S_5X_6$ monolayer are all reduced, as detailed in Table S3. A reasonable explanation for this phenomenon can be provided from the perspective of bonding strength. After removing the S atoms at the vertices, the adjacent Sc atoms lose part of their bonding interactions, resulting in a significant reduction in local bonding strength. This change directly weakens the material's ability to resist tensile and compressive deformations, thereby leading to a decrease in the overall stiffness of the material.

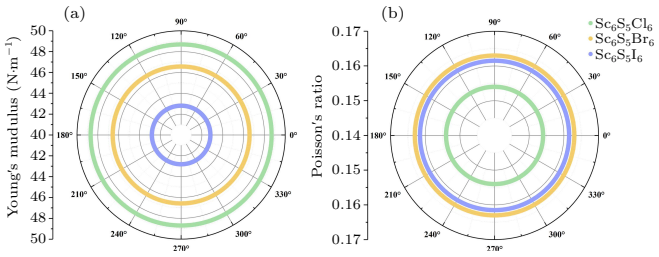


Fig. 3. The calculated angle-dependent in-plane (a) Young's modulus and (b) Poisson's ratio of $Sc_6S_5X_6$.

3.2. Bonding properties

Given the unique structural characteristics of the monolayer $Sc_6S_5X_6$, it is particularly essential to conduct an in-depth exploration of its bonding properties. To this end, the bonding features of the $Sc_6S_5X_6$ monolayer have been systematically investigated using advanced techniques such as the electron localization function (ELF),[45] Bader charge analysis,[46] and crystal orbital Hamiltonian population (COHP).[38] Figure 4(a) presents the ELF results for $Sc_6S_5X_6$. As can be observed from the figure, the charge is predominantly concentrated around the S and halogen atoms, while the electron density near the Sc atoms is almost negligible. These results strongly indicate the formation of predominantly ionic bonding between the Sc atoms and the S/X atoms.

Figure 4(b) and Table 2 present the results of the Bader charge analysis. Within this analytical framework, negative and positive values represent electron loss and electron gain, respectively. The analysis reveals that each Sc atom transfers approximately 2.07e to 2.12e (electrons) to the nearest non-metal atoms. Notably, there is a clear correlation between the number of electrons gained by non-metal atoms and their electronegativity. As the electronegativity gradually decreases from $Sc_6S_5Cl_6$ to $Sc_6S_5I_6$, the number of electrons gained by the halogen atoms decreases accordingly; conversely, the number of electrons gained by the S1 and S2 atoms exhibits an increasing trend.

Table 2. The Bader charge results of $Sc_6S_5X_6$ monolayers. The "+" represents gaining electrons, while "−" represents losing electrons.

Materials	Bader charge (e)			
	Sc	S1	S2	X
$Sc_6S_5Cl_6$	−2.12	+1.46	+1.61	+0.83
$Sc_6S_5Br_6$	−2.09	+1.48	+1.62	+0.79
$Sc_6S_5I_6$	−2.07	+1.50	+1.66	+0.74

Furthermore, the Bader charges of the $Sc_6S_5X_6$ and $Sc_6S_6X_6$ monolayers have been compared, with the corresponding data summarized inTable S4. After the removal of the S3 atom, pronounced changes occur in the electron distribution within the unit cell: the number of electrons lost by the Sc atoms decreases by 0.14e to 0.16e; the electron gain or loss of the S1 atoms remains largely unchanged; the number of electrons gained by the S2 atoms increases by 0.13e to 0.15e; and the number of electrons gained by the halogen atoms increases by 0.04e to 0.06e. These results clearly demonstrate that the removal of the S3 atom induces a redistribution of electrons within the unit cell. In particular, the electron redistribution is more pronounced for the sulfur atoms (S2) in the S-vacancy layer and the Sc atoms originally bonded to the S3 atom, whereas the electron gain or loss of atoms farther from the S vacancy (S1 and halogen atoms) is relatively less affected.

Subsequently, the COHP method has been employed to perform an in-depth analysis of the bonding and antibonding characteristics of the $Sc_6S_5X_6$ monolayer, with the results shown in Figs. 4(c)–4(e). The COHP results clearly indicate that the bonding states between the Sc atoms and the S/X atoms dominate below the Fermi level. In contrast, the COHP of the Sc–Sc bonds is mainly distributed above the Fermi level and exhibits mixed bonding and antibonding

characteristics. Notably, compared with the COHP results of the $Sc_6S_6X_6$ monolayer, additional Sc–S1 antibonding states emerge within the energy range from −2 eV to 0 eV below the Fermi level. This indicates that partial occupation of these antibonding states weakens the interatomic interactions, leading to an elongation of the Sc–S1 bond lengths. Based on the above analysis, it can be concluded that the introduction of S vacancies reduces the bonding stability of $Sc_6S_5X_6$ compared with $Sc_6S_6X_6$, which is fully consistent with the previously discussed thermal stability and related results.

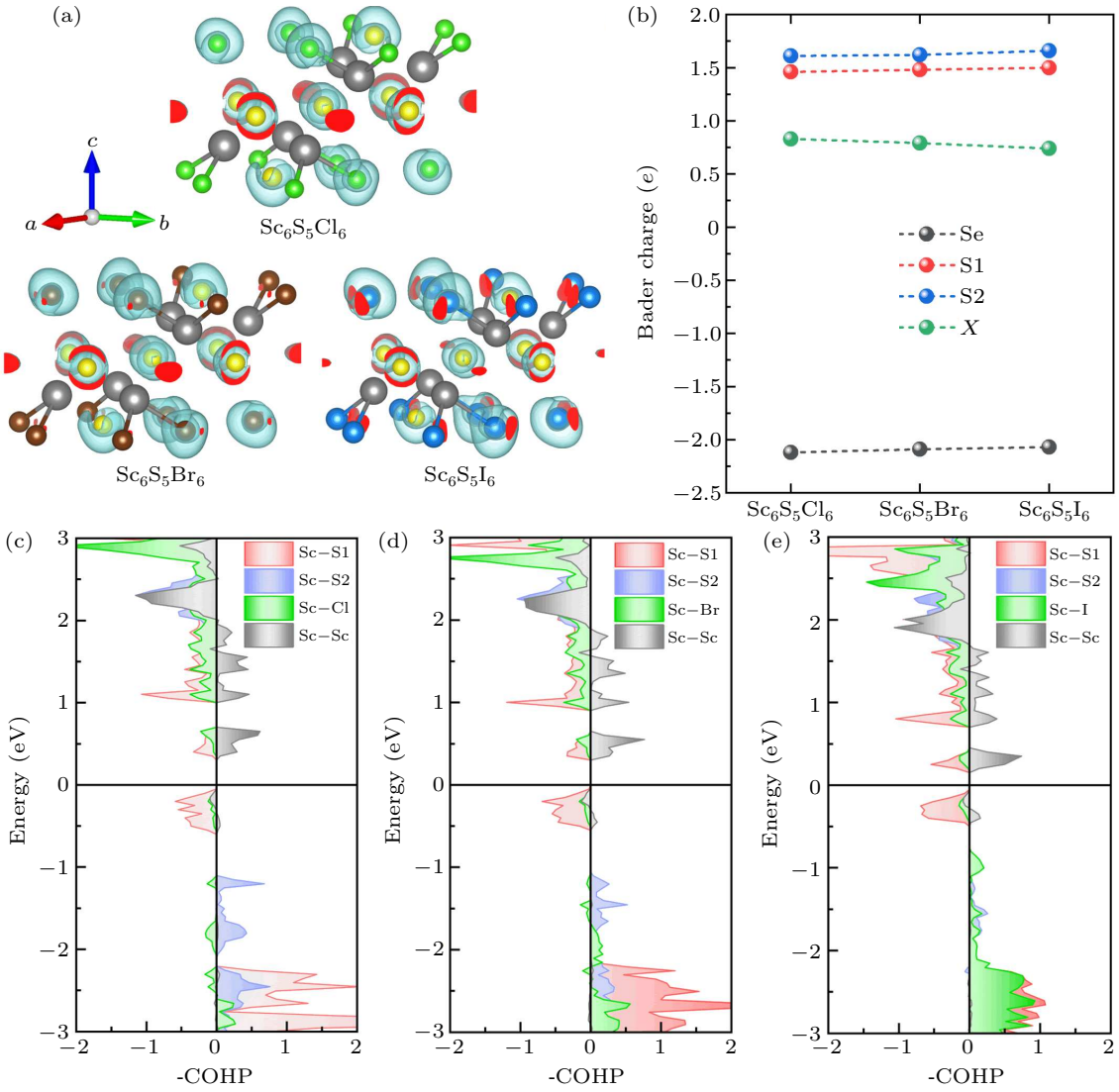


Fig. 4. (a) ELF results of $Sc_6S_5X_6$, (b) Bader charge results of the $Sc_6S_5X_6$, and COHP results of (c) $Sc_6S_5Cl_6$, (d) $Sc_6S_5Br_6$, and (e) $Sc_6S_5I_6$.

3.3. Electronic properties

In the aforementioned content, we have successfully unveiled a series of key microscopic features of the 2D $Sc_6S_5X_6$ system: the removal of the S3 atom induces local lattice distortion and charge redistribution. Specifically, the charge loss of the Sc atoms decreases by 15%, while the electrons gained by the S2 atoms and halogen atoms increase by 9% and 7%, respectively. To further elucidate how such structural reconstruction regulates the macroscopic properties of the material, it is therefore essential to analyze the evolution of its electronic structure.

Firstly, the GGA+PBE functional has been employed to calculate the electronic band structures of monolayer $Sc_6S_5X_6$, with the corresponding results shown in Fig. S3. The calculated band gap values of $Sc_6S_5Cl_6$, $Sc_6S_5Br_6$, and $Sc_6S_5I_6$ are 0.46 eV, 0.43 eV, and 0.33 eV, respectively. However, it should be noted that, due to the intrinsic limitations of the GGA-PBE method, its accuracy in predicting the band gaps of semiconductors and insulators is generally limited.[47–50] To obtain more reliable results, the HSE06 hybrid functional has been further adopted to calculate the band structures of $Sc_6S_5X_6$, as shown in Fig. S4. In comparison with the GGA-PBE results, the HSE06 calculations yield significantly larger band gaps, increasing to 0.97 eV, 0.92 eV, and 0.75 eV for $Sc_6S_5Cl_6$, $Sc_6S_5Br_6$, and $Sc_6S_5I_6$, respectively.

Considering that the monolayer $Sc_6S_5X_6$ contains rela-

tively heavy elements, the influence of spin–orbit coupling (SOC) on the band structure has also been investigated, with the results shown in Figs. 5(a)–5(c). Consistent with the GGA-PBE and HSE06 results, all $Sc_6S_5X_6$ monolayers exhibit indirect band gap characteristics, with the valence band maximum (VBM) located at the *K* point and the conduction band minimum (CBM) at the *M* point. Further analysis indicates that the SOC effect has only a minor influence on the band gap, resulting in a band gap variation of approximately 0.01 eV. More detailed information can be found in Fig. 5(d) and Table 1. Figure 5(e) shows the density of states (DOS) of the monolayer $Sc_6S_5Cl_6$. It can be clearly seen that the valence and conduction bands near the Fermi level are mainly contributed by the Sc-d orbitals (marked in purple and blue in the band structure, respectively). In addition, a sharp peak appears at approximately −1.5 eV below the Fermi level, corresponding to an extremely flat band in the band structure (marked in orange), which is predominantly derived from the S2-p orbitals. Figure 5(f) presents the spatial charge density distributions of the VBM and CBM in the monolayer $Sc_6S_5Cl_6$. The results indicate that the charge densities of both the VBM and CBM are mainly localized around the Sc atoms, in good agreement with the electronic structure analysis. Moreover, for the VBM, a pronounced coupling between the two Sc-based kagome layers is observed at the original position of the S3 atom. This observation clearly demonstrates that the introduction of S3 vacancies significantly modifies the electron density distribution, thereby exerting a pronounced influence on the electronic structure of the monolayer.

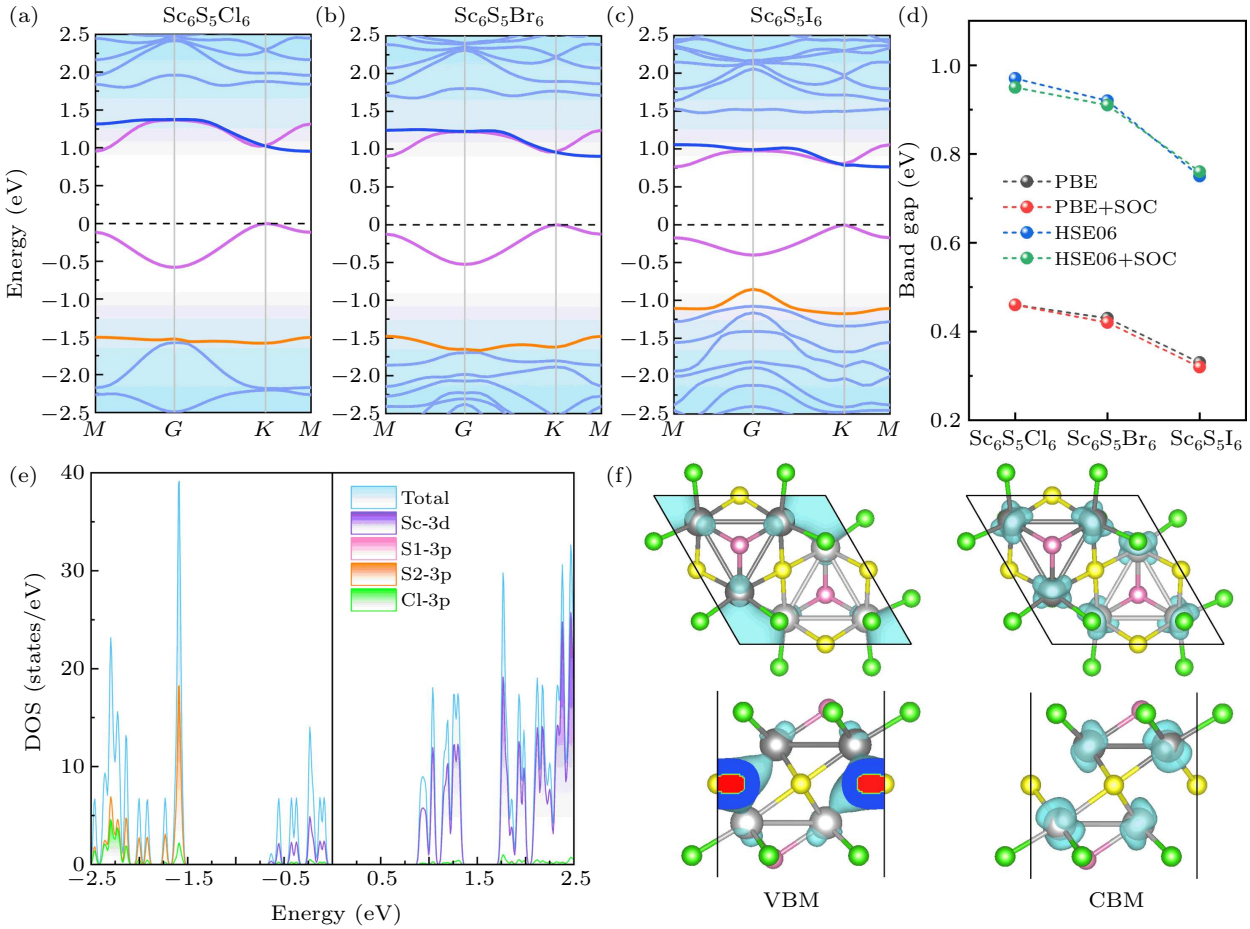


Fig. 5. Electronic band structures of (a) $Sc_6S_5Cl_6$, (b) $Sc_6S_5Br_6$, and (c) $Sc_6S_5I_6$ calculated at the HSE06+SOC level. (d) Band gaps of $Sc_6S_5X_6$ obtained using various computational methods. (e) DOS of $Sc_6S_5Cl_6$. (f) Spatial charge density distributions of the VBM and CBM in $Sc_6S_5Cl_6$ with an isosurface value of 0.03 $e{\cdot}Å^{-3}$.

Subsequently, taking $Sc_6S_5Cl_6$ as a representative example, the orbital contributions to the band structure have been further analyzed, with the results shown in Fig. 6. In the energy range between −1 eV and 3 eV, the bands are predominantly derived from the Sc-d orbitals, whereas the contributions of the non-metal atoms in this region are negligible. More specifically, the isolated bands near the Fermi level originate mainly from the Sc-d_{xz} and Sc-d_{yz} orbitals, while the flat bands above the Fermi level are primarily contributed by the Sc-d_{z^2}, Sc-d_{xz}, and Sc-d_{yz} orbitals. In the lower energy region of the valence band (−2.5 eV to −1 eV), the S2-p_x and S2-p_y orbitals contribute to the flat bands associated with the sulfur-based kagome lattice. For even lower energy valence bands (below −2.5 eV), the states are mainly generated by the coupling between S1-p and Cl-p orbitals, with the S1-p_z orbital and Cl-p_x and Cl-p_y orbitals playing a dominant role.

Through comparative analysis, it is found that, compared with the monolayer $Sc_6S_6X_6$, the Fermi level in the $Sc_6S_5X_6$ band structure shifts upward, as shown in Fig. S5. Combined with the Bader charge analysis, it is evident that the removal of the S3 atom releases the electrons originally bonded to it, leading to a spatial redistribution of charges. Specifically, Sc atoms gain some electrons compared to the pristine system (i.e., the number of electrons lost decreases), while S2 and halogen atoms also gain additional electrons. Therefore, the introduction of S vacancies effectively acts as donor defects, injecting extra electrons into the system and increasing the overall electron concentration. In terms of the electronic structure, this manifests as enhanced electron filling of the Sc-d and S2-p orbitals, which lowers the energy of the corresponding bands and results in a downward shift of the valence and conduction bands near the Fermi level. At the same time, the increased electron occupation enhances the density of states, reduces the band curvature, and increases the electron effective mass, leading to flatter bands. Moreover, the introduction of S vacancies breaks the lattice symmetry, causing the two originally quadratic bands that formed Dirac points at the *K* point to separate and open a gap at the Dirac points.

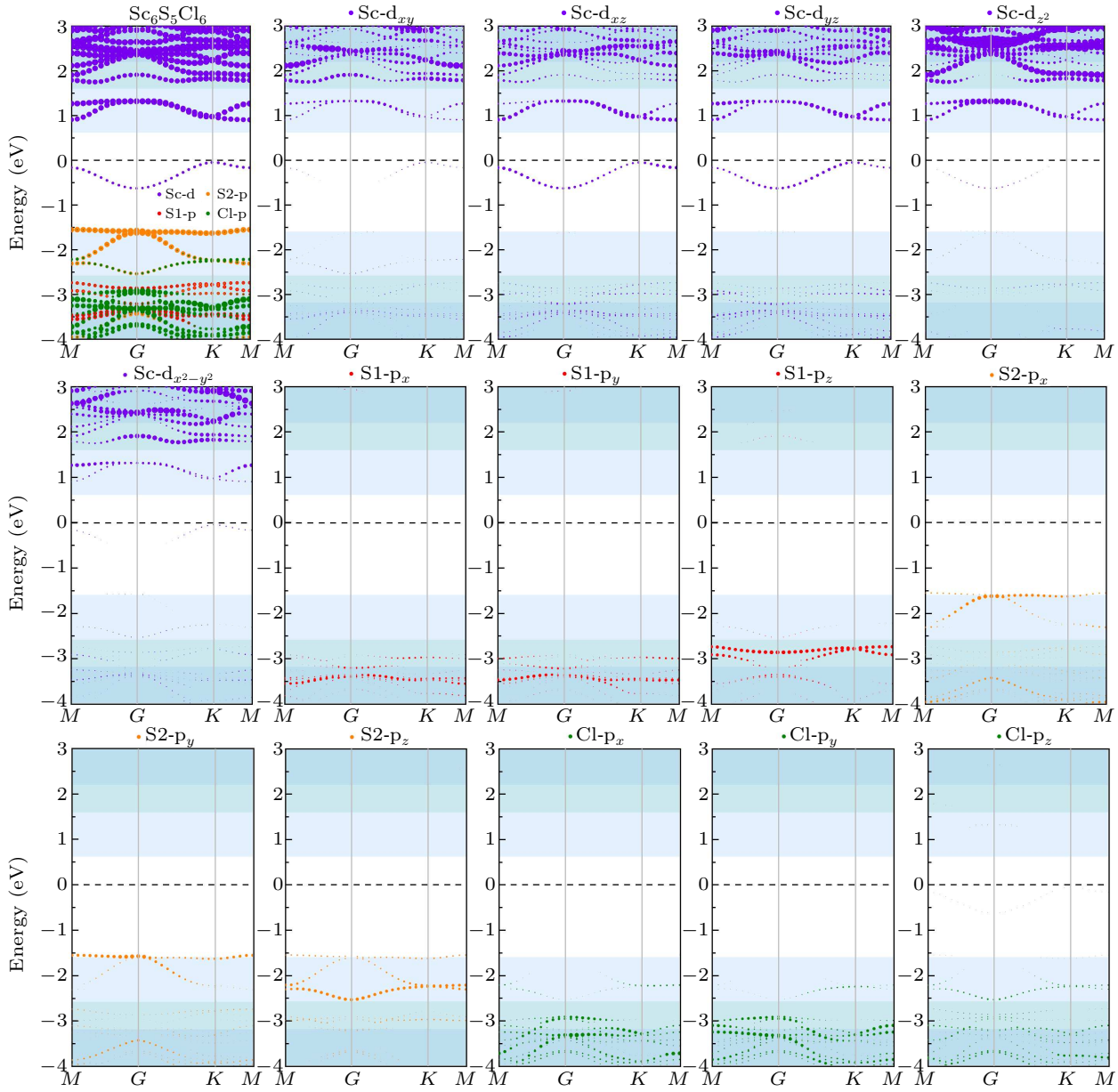


Fig. 6. Projected band structures of $Sc_6S_5Cl_6$ based on HSE06+SOC calculations.

3.4. Carrier mobility

Finally, we focus on the carrier mobility of the 2D $Sc_6S_5X_6$ monolayer, which is a crucial factor in evaluating the material's potential for device applications. Currently, the deformation potential theory proposed by Bardeen and Shockley[51] (hereafter referred to as the BS theory) is the

most widely used approach for assessing carrier mobility. However, the conventional BS theory has certain limitations, as it does not account for anisotropy in the material. To obtain more accurate carrier mobility values, we employed the anisotropy-corrected BS method proposed by Lang *et al.*[52] to evaluate $Sc_6S_5X_6$. For comparative purposes, the results obtained using the standard BS theory are also presented. Detailed information regarding the computational procedures can be found in Note 2 of the supplementary materials.

As shown in Fig. 7 and Table S5, the calculated carrier effective masses and mobilities of monolayer $Sc_6S_5X_6$ are summarized. For holes, the effective masses exhibit minor variation, ranging from $0.72m_0$ to $0.87m_0$ (where m_0 is the rest mass of a free electron), which are relatively low compared to the electron effective masses. However, owing to relatively high deformation potential energies, ranging from 1.13 eV to 1.77 eV, the hole mobilities remain moderate, with values between 482.64 $cm^2{\cdot}V^{-1}{\cdot}s^{-1}$ and 930.26 $cm^2{\cdot}V^{-1}{\cdot}s^{-1}$.

In contrast, the electron effective masses show more pronounced anisotropy. Along the *a*-direction, the electron effective masses range from $0.83m_0$ to $1.29m_0$, while along the *b*-direction, they are generally larger, exceeding $2m_0$ in most cases. Notably, for $Sc_6S_5I_6$, the electron effective mass reaches $50.64m_0$. Such a large effective mass is primarily attributed to the relatively flat band structure in this system, which in turn results in a very low carrier mobility of 6.73 $cm^2{\cdot}V^{-1}{\cdot}s^{-1}$.

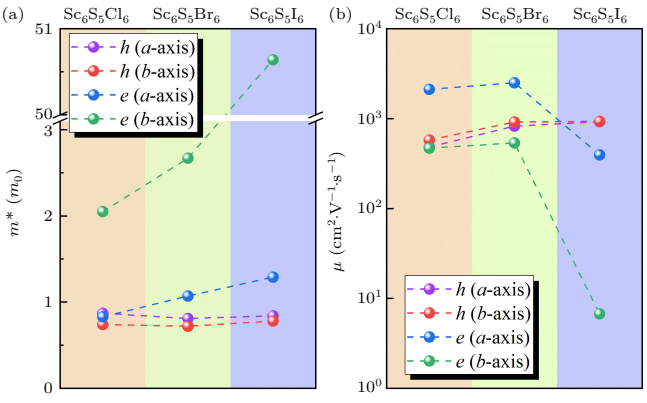


Fig. 7. The calculated (a) carrier effective masses (*e* for electron, *h* for hole), and (b) carrier mobility of $Sc_6S_5X_6$.

It can be observed that for monolayer $Sc_6S_5Cl_6$ and $Sc_6S_5Br_6$, when oriented along the *a*-direction, both the electron effective mass and the deformation potential energy are relatively low, ranging from 0.16 eV to 0.26 eV. As a result, the electron mobility of these two materials is comparatively high, exceeding 10^3 $cm^2{\cdot}V^{-1}{\cdot}s^{-1}$ (2114.21 $cm^2{\cdot}V^{-1}{\cdot}s^{-1}$ for $Sc_6S_5Cl_6$ and 2505.33 $cm^2{\cdot}V^{-1}{\cdot}s^{-1}$ for $Sc_6S_5Br_6$). For additional data on carrier mobility, refer to Table S5 in the supplementary materials.

4. Conclusion

In summary, we have employed an innovative strategy by precisely introducing sulfur vacancies at specific sites in $Sc_6S_6X_6$, thereby constructing a novel 2D kagome semiconductor, $Sc_6S_5X_6$ (X = Cl, Br, I), featuring three kagome layers. Theoretical calculations reveal that the incorporation of S vacancies induces substantial structural reorganization, including the elongation of bond lengths and the expansion of lattice constants. More importantly, this structural modification results in a reduction of thermodynamic stability at elevated temperatures due to the emergence of local compressive stress.

In terms of mechanical properties, the presence of S vacancies decreases both the Young's modulus and Poisson's ratio, significantly enhancing the material's flexibility. This effect is attributed to the reduced bonding density in the vacancy regions and the partial occupation of antibonding states in the Sc–S1 bonds.

The electronic structure is profoundly affected as well. Acting as donor defects, the S vacancies trigger charge redistribution, resulting in a reduction of the band gap to 0.76–0.95 eV and a transformation in the semiconductor band type. The kagome bands contributed by the Sc-based kagome lattices are predominantly located near the Fermi level. Additionally, the disruption of lattice symmetry induces the opening of a band gap at the Dirac points. Regarding carrier mobility, with the exception of $Sc_6S_5I_6$, which exhibits extremely low electron mobility due to its excessively large effective mass, the remaining monolayers demonstrate favorable electron and hole mobilities within the range of 10^2–10^3 $cm^2{\cdot}V^{-1}{\cdot}s^{-1}$.

Overall, our work not only highlights the potential application prospects of the 2D kagome semiconductor $Sc_6S_5X_6$ in electronic devices, but also provides a practical paradigm for constructing novel 2D multilayer kagome materials, laying a solid foundation for future development in this field.

Acknowledgment

This project was supported by the Fundamental Research Funds for the Central Universities (WUT: 2024IVA052 and Grant No. 104972025KFYjc0089).

References

[1] Zhang G, Wu H, Jin W, Yang L, Xiao B, Yu J, Zhang W and Chang H 2025 *Cell Rep. Phys. Sci.* **6** 102356
[2] Liu A, Zhang X, Liu Z, Li Y, Peng X, Li X, Qin Y, Hu C, Qiu Y, Jiang H, Wang Y, Li Y, Tang J, Liu J, Guo H, Deng T, Peng S, Tian H and Ren T L 2024 *Nano-Micro Lett.* **16** 119
[3] Tong L, Peng Z, Lin R, Li Z, Wang Y, Huang X, Xue K H, Xu H, Liu F, Xia H, Wang P, Xu M, Xiong W, Hu W, Xu J, Zhang X, Ye L and Miao X 2021 *Science* **373** 1353
[4] Du L 2024 *Nat. Rev. Phys.* **6** 157
[5] Shuck C E, Xiao X and Wang Z 2024 *Acc. Chem. Res.* **57** 3079

[6] Wilson N P, Yao W, Shan J and Xu X 2021 *Nature* **599** 383
[7] Zhou Y and Zhao L 2017 *Adv. Mater.* **29** 1702676
[8] Wang Q, Lei H, Qi Y and Felser C 2024 *Acc. Mater. Res.* **5** 786
[9] Li S 2025 *Chinese Phys. Lett.* **42** 070716
[10] Mendels P, Bert F, De Vries M A, Olariu A, Harrison A, Duc F, Trombe J C, Lord J S, Amato A and Baines C 2007 *Phys. Rev. Lett.* **98** 077204
[11] Yin J X, Lian B and Hasan M Z 2022 *Nature* **612** 647
[12] Jiang K, Wu T, Yin J X, Wang Z, Hasan M Z, Wilson S D, Chen X and Hu J 2022 *Natl. Sci. Rev.* nwac199
[13] Jiang H C, Devereaux T and Kivelson S A 2017 *Phys. Rev. Lett.* **119** 067002
[14] Xu X, Yin J X, Qu Z and Jia S 2023 *Rep. Prog. Phys.* **86** 114502
[15] Chen H, Hu B, Ye Y, Yang H and Gao H J 2022 *Chin. Phys. B* **31** 097405
[16] Ye J, Lin Y, Wang H, Song Z, Feng J, Xie W and Jia S 2024 *Chin. Phys. B* **33** 057103
[17] Zhou H, Liu H, Ji H, Li X, Meng S and Sun J T 2023 *npj Quantum Mater.* **8** 16
[18] Regmi S, Fernando T, Zhao Y, Sakhya A P, Dhakal G, Bin Elius I, Vazquez H, Denlinger J D, Yang J, Chu J H, Xu X, Cao T and Neupane M 2022 *Commun. Mater.* **3** 100
[19] Lu J, Chen H, Zhao X, Hu G, Yuan X and Ren J 2024 *Appl. Phys. Lett.* **124** 072101
[20] Li Y, Liu C, Zhao G D, Hu T and Ren W 2021 *Phys. Rev. B* **104** L060405
[21] You J Y and Feng Y P 2023 *Mater. Today Chem.* **30** 101566
[22] Wang H and Yang L 2024 *J. Phys. Chem. Lett.* **15** 8689
[23] Wang R, Wang C, Li R, Guo D, Dai J, Zong C, Zhang W and Ji W 2025 *Chin. Phys. B* **34** 046801
[24] Huang S, Xie Y, Zhong C and Chen Y 2018 *J. Phys. Chem. Lett.* **9** 2751
[25] Li J, Wang X T, Chen Y Q, Wei Y H, Yuan H K and Tian C L 2024 *Phys. Chem. Chem. Phys.* **26** 3092
[26] Wu D, Lv H, Zhuo Z, Li X, Wu X and Yang J 2021 *J. Phys. Chem. Lett.* **12** 3528
[27] Zhang B, Deng F, Chen X, Lv X and Wang J 2022 *J. Phys.: Condens. Matter* **34** 475702
[28] Park S, Kang S, Kim H, Lee K H, Kim P, Sim S, Lee N, Karuppannan B, Kim J, Kim J, Sim K I, Coak M J, Noda Y, Park C H, Kim J H and Park J G 2020 *Sci. Rep.* **10** 20998
[29] Zhu Y, Yuan J H and Wang J 2025 *Phys. B Cond. Matt.* **700** 416894
[30] Zhu Y, Yuan J H and Wang J 2025 *Appl. Surf. Sci.* **709** 163829
[31] Zhu Y, Yuan J H, Fang W Y, Sun Z G and Wang J 2023 *Appl. Surf. Sci.* **636** 157817
[32] Yan J L, Wang X Y, Chen L, Yuan J H, Ke Y J and Wang J 2025 *Mater. Today Commun.* **48** 113650
[33] Blöchl P E 1994 *Phys. Rev. B* **50** 17953
[34] Kresse G and Joubert D 1999 *Phys. Rev. B* **59** 1758
[35] Kresse G and Furthmüller J 1996 *Comput. Mater. Sci.* **6** 15
[36] Kresse G and Furthmüller J 1996 *Phys. Rev. B* **54** 11169
[37] Perdew J P, Burke K and Ernzerhof M 1996 *Phys. Rev. Lett.* **77** 3865
[38] Nelson R, Ertural C, George J, Deringer V L, Hautier G and Dronskowski R 2020 *J. Comput. Chem.* **41** 1931
[39] Togo A and Tanaka I 2015 *Scripta Mater.* **108** 1
[40] Wang V, Xu N, Liu J C, Tang G and Geng W T 2021 *Comput. Phys. Commun.* **267** 108033
[41] Born M and Huang K 1996 *Dynamical Theory of Crystal Lattices* (New York: Oxford University Press)
[42] Li T 2012 *Phys. Rev. B* **85** 235407
[43] Liu F, Ming P and Li J 2007 *Phys. Rev. B* **76** 064120
[44] Yuan J, Yu N, Xue K and Miao X 2017 *RSC Adv.* **7** 8654
[45] Noury S, Krokidis X, Fuster F and Silvi B 1999 *Comput. Chem.* **23** 597
[46] Tang W, Sanville E and Henkelman G 2009 *J. Phys. Condens. Matter* **21** 084204
[47] Mao G Q, Yan Z Y, Xue K H, Ai Z, Yang S, Cui H, Yuan J H, Ren T L and Miao X 2022 *J. Phys.: Condens. Matter* **34** 403001
[48] Yang S, Xue K H and Miao X 2025 *J. Phys.: Condens. Matter* **37** 233001
[49] Yuan J H, Chen Q, Fonseca L R C, Xu M, Xue K H and Miao X S 2018 *J. Phys. Commun.* **2** 105005
[50] Xue K H, Yuan J H, Fonseca L R C and Miao X S 2018 *Comput. Mater. Sci.* **153** 493
[51] Bardeen J and Shockley W 1950 *Phys. Rev.* **80** 72
[52] Lang H, Zhang S and Liu Z 2016 *Phys. Rev. B* **94** 235306